Materials & Design 268 (2026) 116584

Contents lists available at ScienceDirect

Materials & Design

journal homepage: www.elsevier.com/locate/matdes

A quasi-zero stiffness biasing mechanism for electrostatic bellow muscle zipping actuators

Hadi Taghvaei [a], Marco Riva [a], Matteo Benedetti [a], Marco Fontana [b], Pasquale Gallo [a,*], Giacomo Moretti [a,*]

[a] Department of Industrial Engineering, University of Trento, Trento, Italy
[b] Institute of Mechanical Intelligence, Scuola Superiore Sant'Anna, Pisa, Italy

HIGHLIGHTS

- A Quasi-Zero Stiffness (QZS) biasing mechanism for zipping electrostatic actuators.
- Computational model and experimental validation of the QZS mechanism.
- Design procedures for the mechanism-actuator system.
- Static and dynamic testing of a coupled actuator–QZS mechanism prototype.

ARTICLE INFO

Keywords:
Electrostatics
Dielectric fluid actuator
Zipping actuator
Quasi–zero stiffness
Biasing mechanism

ABSTRACT

Electrostatic zipping actuators are electromechanical drives capable of large voltage-induced deformations, with promising applications in soft robotics and wearable mechatronics. To produce a stroke, certain zipping actuator topologies need to be preloaded by an external force, producing a deformation that is then counteracted by electrostatic forces. This study presents a concept for a quasi-zero stiffness (QZS) biasing mechanism for zipping actuators and demonstrates its integration in a family of contractile actuators known as electrostatic bellow muscles (EBMs). The mechanism uses preloaded buckling beams to provide a nearly constant preload force, which reopens the actuator after each actuation cycle without increasing stiffness in operation. Under large external tensile loads, the beams transition into a load-bearing state that limits additional extension, acting as mechanical constraints that protect the actuator from failure. In this work, a model and design guidelines for the QZS mechanism are developed, along with a prototype of a coupled EBM–QZS mechanism system in which the biasing mechanism adds less than 10% weight to the actuator mass. Tests demonstrated that the EBM-QZS system provides a nearly constant low-force stroke without compromising the EBM frequency response, while preserving structural integrity under external forces tens of times larger than the EBM's weight.

1. Introduction

In the last few years, electrostatic zipping actuators based on flexible polymeric dielectrics [1–3] have emerged as a key enabling technology for new robotic and mechatronic devices [4–6], as they hold the potential to promote a paradigm shift towards fully-soft and lightweight solutions [7]. Functionally, zipping actuators are variable capacitors based on a multilayer structure combining flexible dielectric polymers and dielectric liquid gaps, which enable the actuators to deform in response to an applied voltage [8].

While in some zipping actuator topologies (known as hydraulically amplified self-healing electrostatic actuators - HASELs) the initial actuator shape (and, hence, its ability to deform in response to a voltage) is provided by the pressurisation of a dielectric fluid in a pouch [2], other devices rely on deformations provided by external forces to produce a stroke. Examples of zipping actuators in this latter class are the so-called electro-ribbons [9], the electrostatic bellow-muscles (EBMs) [9], or the honeycomb zipping actuator [10]. These devices typically feature stackable architectures with initially-flat densely packed units, which allow achieving large actuation strains, but rely on external forces to create an

* Corresponding authors.
Email addresses: pasquale.gallo@unitn.it (P. Gallo), giacomo.moretti@unitn.it (G. Moretti).

https://doi.org/10.1016/j.matdes.2026.116584
Received 4 May 2026; Received in revised form 30 June 2026; Accepted 12 July 2026
Available online 14 July 2026

initial gap between the electrodes and enable the onset of the zipping process.

Among them, the EBM introduced by Sîrbu et al. [11,12] is a promising concept that features a compact design that guarantees dielectric fluid encapsulation, can be manufactured easily using scalable procedures, and enables different working modes, including operation as contractile actuator and pump. Besides actuator operation, the EBM has been demonstrated to work as an energy harvester [13] capable of cyclically converting mechanical work into electrical energy [11]. Liquid-free realisations of the EBM have recently been proposed as actuators for space applications, leveraging ultra-low pressure atmospheres (vacuum) as functional materials for the dielectric gaps [12].

In previous works, preloading of cellular or lattice electrostatic actuators has been addressed by providing the actuator's flexible walls (holding the flexible dielectric layers) with a bending stiffness (sufficient to provide a restoring force to re-open the actuator upon zipping) and a pre-deformation (to create an open gap in the absence of external forces) [14–16]. This solution comes at the cost of increased manufacturing complexity and is not applicable in actuators that use stretching (rather than bending) of the dielectric polymer layers, such as the EBM. In applications such as grippers [12,17], moving robots [18], or robotic platforms [19], actuator preloading has been provided by leveraging the stiffness of the coupled robotic structure, on a case-specific basis.

In the field of electrostatic actuators, the use of biasing springs has been extensively pursued in combination with dielectric elastomer actuators [20] (which require a pre-stretch or an out-of-plane preload to function correctly) to deliver self-standing units capable of providing actuation regardless of a specific coupling layout [21,22]. A group of researchers at Saarland University, in particular, proposed the use of negative-stiffness biasing springs for dielectric elastomers, implemented via pre-compressed buckled beams [23], polymeric domes [24], or pre-deformed thermoplastic beams [25]. In contrast to positive rate springs, negative or quasi-zero stiffness (QZS) springs can provide preload without increasing the overall system stiffness, which would otherwise significantly reduce the actuator's stroke capability [22]. Negative-stiffness mechanisms, in particular, have been extensively used in dielectric elastomer actuators to compensate for the positive stiffness of the elastomer membrane and allow larger stroke generation. Since DEAs' dimensional envelope is mainly governed by the radial size (i.e., the dimensions parallel to the electrode surface), negative-stiffness biasing springs for DEAs have transverse dimensions that are typically longer than their longitudinal dimensions, and they are stacked with the actuator, thus increasing its dimensional footprint and decreasing its percentage contraction capability.

Different embodiments of QZS mechanisms have been proposed and demonstrated in the past, especially for applications in the field of vibration isolation [26–28]. In this latter field, QZS mechanisms are technically relevant because they feature high stiffness (referred to as static stiffness) in the neighborhood of the equilibrium configuration, and low stiffness (dynamic stiffness) over a broad portion of the working range, and allow reducing the system natural frequency while retaining a high load bearing capacity.

While some concepts of QZS mechanisms (especially at large scales) are developed using articulated structures with rigid links and springs [29,30], other concepts rely on flexible mechanisms [26]. While the simplest prototypical version of negative or QZS mechanisms consists of buckled beams pre-compressed along their axis (perpendicular to the spring working direction) [31], a broad variety of design solutions based on bending beams and tailored mechanical metamaterials has been proposed in the past [32,33]. QZS mechanisms, in particular, have typically been designed using curved beams [34], such as arc-shaped beams [28], or inclined [35] beam geometries, in which non-straight beam shapes are obtained either by additive manufacturing, or by permanent deformation of straight beams [36,37]. Several QZS structures have been devised by integrating curved positive-stiffness and negative stiffness elements within the same monolithic structure or multi-cell metamaterial [28], typically by resorting to additive manufacturing methods [38–40]. In other settings, QZS mechanisms have been obtained by incorporating stiffness contributions induced by magnetic forces [41].

In this article, we propose a concept of a QZS biasing mechanism for electrostatic zipping actuators, and devise design strategies to couple it with EBMs. The proposed QZS biasing mechanism has the dual function of 1) providing the actuator with a preload (and, hence, the capability to provide a free displacement when low or no external tensile forces are applied), and 2) limiting the actuator strain (hence avoiding structural damage) in the presence of large external tensile forces. The mechanism layout is devised to envelop the EBM, without increasing its longitudinal length and, hence, without reducing its percentage contraction capability. Similar to Euler springs [42,43], the mechanism relies on compression buckling of a set of beams, and it consists of a set of slender beams mounted in a configuration that provides them with a self-balanced bent shape. In contrast to similar QZS systems presented in the past [44], which relied on initially-curved beams, our proposed mechanism is obtained starting from flat beams, which are brought into a buckled configuration by mutual preloading during mounting, with no plastic deformations involved. Compared to solutions with thermo-formed beams [25], this solution is easier to manufacture and less prone to mounting/tolerance errors. Compared to 3D-printed QZS springs [36], our design allows the use of thin laminated beams made of structural-grade polymeric materials - a solution that offers better reliability, higher elastic energy density, and lower hysteresis in dynamic working conditions.

Here we present a study of the dependence of the QZS mechanism force response on geometrical and design parameters, based on the elastica theory [45]. Building upon model-based design guidelines, a design of an integrated EBM with a QZS mechanism is presented, which relies on an EBM embodiment similar to that introduced in [11], and a QZS with bending beams made of thin biaxially oriented polyethylene terephthalate (BoPET) sheets. Static and dynamic experiments show that the proposed QZS mechanism enables the EBM to achieve a finite stroke at low loads, while protecting the actuator from overstretching under large external tensile forces. Compared to a base EBM design (with no biasing mechanism), the weight increase due to the QZS mechanism is less than 10% and is fully ascribable to structural/connection elements (which could be further optimised and improved), with a negligible contribution from the polymeric beams.

The article is organized as follows. Section 2 introduces the EBM and the QZS mechanism layout, and discusses coupling design trade-offs. Section 3 introduces an analytical model for the QZS mechanism. Section 4 describes the experimental setups and procedures. Section 5 discusses results from experimental testing of the QZS mechanism and the integrated EBM–QZS mechanism system. Finally, conclusions are presented in Section 6.

2. Quasi-zero stiffness preloading mechanism for EBMs: layout and working principle

This section presents the design and operating principles of the proposed actuator system, combining an electrostatic bellow muscle (EBM) with a quasi-zero-stiffness (QZS) mechanism. First, the working principle and structural features of the EBM are described, highlighting its limitations in terms of load-dependent actuation. Subsequently, the QZS mechanism is introduced as a biasing strategy to enable finite stroke under zero external load and to shape the overall force–displacement response. The coupling between the two subsystems is then analyzed, with particular attention to the resulting equilibrium conditions and performance trade-offs.

2.1. The electrostatic bellow muscle (EBM)

The EBM is a dielectric fluid zipping actuator that features a modular structure with multiple actuation units arranged to form a stack [11]. A single EBM unit is composed of initially flat circular polymeric

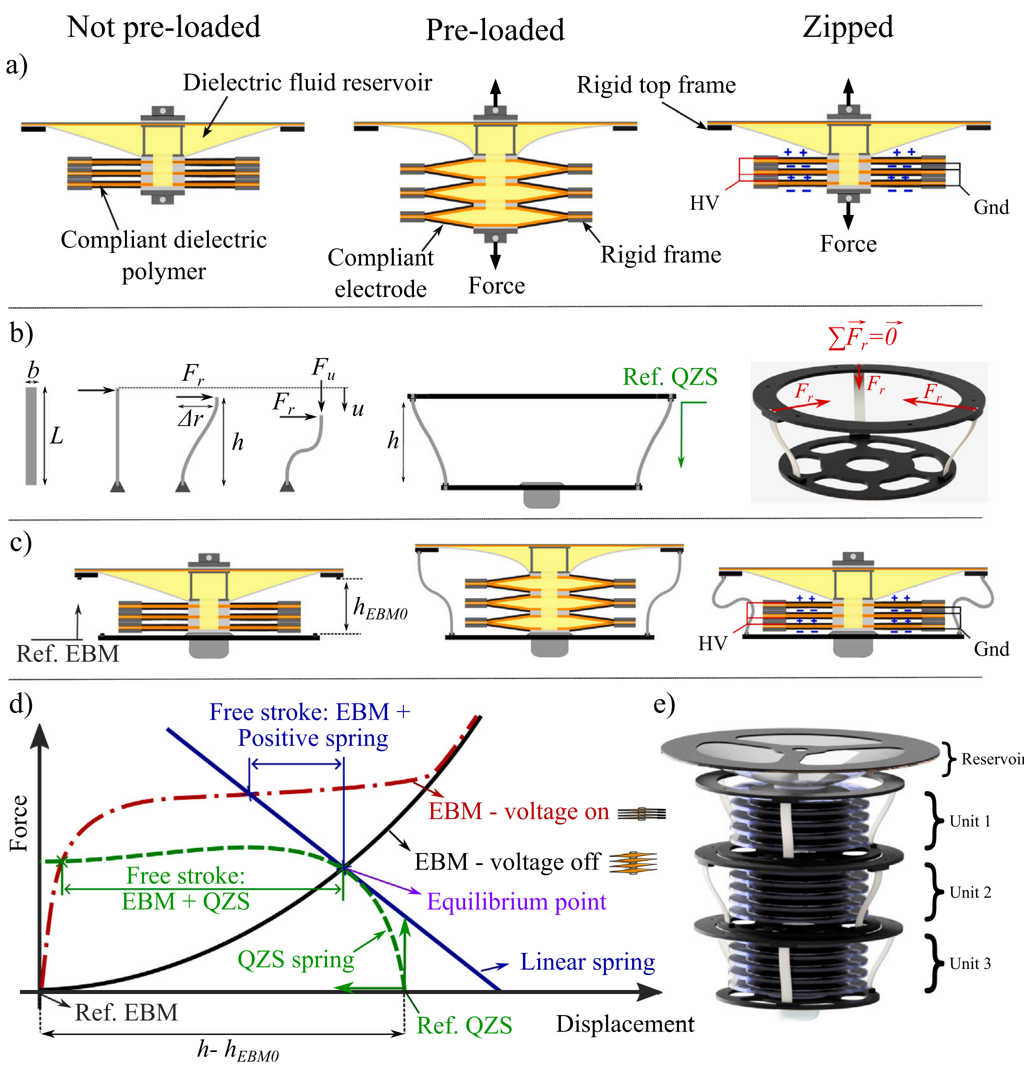

Fig. 1. (a) Working principle of a 3-unit EBM stack. Main components: dielectric polymer chamber, compliant electrodes, rigid annular frames, and fluid reservoir; **(b)** Layout of the proposed QZS mechanism, composed of pre-bent radial beams undergoing buckling under compression; **(c)** Coupling between a QZS mechanism and a 3-unit EBM; **(d)** Qualitative comparison between linear and QZS biasing elements: the force–displacement diagram reports the static response of the EBM (passive or with a voltage applied) and that of a coupled biasing mechanism (linear spring or QZS mechanism). The intersections represent equilibrium points; **(e)** Conceptual layout for a large multi-unit EBM stack with modular QZS units.

dielectric films, which form the walls of a variable chamber that contains a dielectric liquid. Compliant electrodes are deposited on the external faces of the films. The membranes are externally supported by circular rigid frames, which constrain the membranes' deformation (Fig. 1a). In the absence of externally applied forces, the unit is flat and virtually no liquid is present between the polymeric dielectric layers. Applying an external tensile force on the polymeric films causes the latter to stretch and assume a truncated cone shape, creating a gap that is filled by the dielectric liquid. The preload is applied through a central disc element connected to the dielectric membranes.

Once a voltage is applied, Maxwell stress causes the electrodes to progressively zip together. This action pushes the liquid into an external reservoir and induces a contraction of the device, which returns toward its flat state. The reservoir consists of a chamber with extensible soft walls that allow volume expansion during device operation. Multiple EBM units can be connected in series, sharing the liquid volume through interconnecting channels. In this configuration, the achievable contraction increases with the number of units composing the device. The cross–section of a 3-units EBM device is shown in Fig. 1(a), together with its different working configurations.

2.2. Biasing mechanism layout

A key limitation of the EBM is that it requires an external load to create a serviceable gap between the electrodes, which would otherwise remain closed due to the stiffness of the membranes.

In particular, the load determines the out-of-plane deformation of the actuator units, which corresponds to the maximum available stroke. To overcome this limitation, in this work a passive elastic biasing element is coupled with the EBM in order to produce a finite stroke even in the absence of an external load. Although different biasing strategies can be adopted, we design a quasi-zero-stiffness (QZS) mechanism with a double role: 1) providing the EBM with a nearly constant preload over a wide portion of the operating range; 2) protecting the device from overstretching under large external loads.

Similar to Euler springs [42], the QZS mechanism is composed of a set of buckled beams that work in compression. As shown in Fig. 1(b), each beam is initially straight (with length L) and is clamped to a rigid frame at the bottom end. The free end is then displaced by Δr perpendicular to the undeformed beam axis, causing elastic bending, and then fixed to a top rigid frame that constrains the beam's transverse motion.

With the goal of obtaining a self-equilibrated structure, multiple beams are arranged at the vertices of a polygon, with their top and bottom ends connected to a common pair of rigid frames. This configuration ensures that the sum of the transverse force components F_r (generated by the imposed transverse displacement and acting perpendicular to the beam axis) is balanced, resulting in a zero resultant in-plane force, as shown in Fig. 1(b).

As shown in Fig. 1(b), the mechanism height h (upon beam bending) in the mounting equilibrium configuration is lower than the initial beams' length L. Due to the beams' pre-buckling, applying a compressive force F_u to the structure leads to a longitudinal compression of the mechanism, which is accommodated by the bending of the beams, and a QZS response. In contrast to that, in the presence of external pulling forces, the beams are subject to tensile loads, but no (or very limited) longitudinal deformation takes place, due to the beams' inextensibility. Since the beam deformation is dominated by bending, the beam length remains approximately constant during deformation, and longitudinal contraction (i.e., a reduction in the distance between the beam ends) is accommodated through an increase in curvature.

2.3. Coupling concept

The QZS mechanism is coupled with the EBM by connecting the mechanism's top and bottom plates (holding the beam ends) to the top and bottom central disks of the EBM. As shown in Fig. 1(b) and (c), the mechanism has an unperturbed height h (corresponding to the distance between the beam ends in the mounting configuration), which is greater than the unstretched EBM thickness h_{EBM0} in order to allow for device preloading.

To illustrate how a biasing elastic element affects the stroke achievable with an EBM, Fig. 1(d) shows a qualitative force–displacement plot of the two coupled elements, namely the EBM and the biasing mechanism. The figure is qualitative and intended for illustrative purposes. The horizontal axis represents the EBM displacement with respect to its flat equilibrium configuration, whereas the vertical axis represents the corresponding restoring force.

The black and red curves respectively represent the elastic response of the EBM (passive), and the response of the EBM in the presence of a constant voltage, using qualitative trends consistent with those observed in previous studies [11,12]. The green dashed curve qualitatively represents the force–displacement behavior of a QZS mechanism, used as a biasing element, while the blue curve represents the response of an alternative generic biasing element with positive stiffness (e.g., a linear spring).

The connection between the actuator and the biasing spring induces a pretensioning in the EBM and a corresponding pre-compression of the QZS mechanism. Mechanically, the coupled system can be regarded as the parallel connection of two springs (the EBM and the biasing element) [22]. Along the horizontal axis, a displacement equal to zero corresponds to a flat position for the EBM. Due to the mutual dimensions, the position in which the QZS biasing mechanism produces zero force is reached in correspondence with a tensile displacement $h - h_{EBM0}$ of the EBM. For displacements lower than $h - h_{EBM0}$, increasing the EBM elongation leads to a decrease in the mechanism compression. The intersection points between the force–displacement curves of the EBM and the response of the biasing element identify the equilibrium configurations of the coupled system (EBM–QZS mechanism), either in the presence or in the absence of an applied voltage. The horizontal distance between those intersection points corresponds to the system stroke in the absence of external loads (i.e., the free stroke).

By comparing the free stroke of the proposed coupled system (EBM–QZS mechanism) with that of an alternative design in which the EBM is coupled with a positive stiffness spring, it is clear that the maximum achievable stroke (free stroke) can be significantly larger in the presence of a QZS mechanism [22].

The choice of the QZS force plateau value (i.e., the biasing force to which the EBM is subjected) represents a trade-off between maximum free displacement—which increases by increasing the EBM preloading—and stroke capability under load, as the EBM blocking force is reduced by the mechanism force.

In this work, the focus is set on integrating a QZS mechanism into a relatively small array, made up of 3 EBM units (as in Fig. 1c), enveloping the fluid reservoir within the active height of the QZS mechanism. The proposed mechanism design, however, lends itself to stacking and modularisation. Fig. 1(e) illustrates a possible design aimed at integrating a larger number of EBMs coupled with the QZS mechanism. The system is conceived as a series of modular units, each consisting of a stack of EBM units coupled with a QZS mechanism. These units are connected in series while sharing a common reservoir. This approach avoids the use of a single QZS unit surrounding a large EBM stack, which would entail two main drawbacks. First, the substantially increased beam length required to accommodate a larger EBM stack would result in large horizontal beam offsets, Δr, leading to a significant increase in the lateral footprint of the device. Second, the increase in beam length would substantially reduce the natural frequency of the beams' bending modes, which is inversely proportional to the square of the beam length. Although this layout involves multiple QZS systems connected in series, it does not introduce the criticalities that are typical of series-connected QZS mechanisms (i.e., sequential non-synchronous snapping of different series elements [33]), since each QZS mechanism is arranged in parallel with an EBM stack. Slight differences among different QZS modules would lead to small differences in the contraction achieved by the individual actuator–mechanism units, without compromising their ability to deform concurrently.

3. Modeling and design of the QZS mechanism

In this section, an analytical model describing the force response of the QZS mechanism is introduced. Modeling is limited to the static behavior of the beams. This choice is justified by the expectation (later confirmed by experiments) that the dynamics of the coupled EBM-mechanism system are governed by the EBM fluid dynamics, rather than the mechanism viscoelasticity and structural damping. The proposed static model is used to investigate the parametric dependence of the mechanism force response on geometrical and material parameters, and to guide the design of the mechanism in order to achieve the desired performance when coupled with the EBM stack.

3.1. Model formulation

To model the static behavior of a single beam, deformed as in Section 2.2, we adopt Euler–Bernoulli's theory, accounting for geometric nonlinearities through the elastica formulation [31,45,46], under the assumption of a flexible but inextensible beam subjected to small strains and large deflections, with a rectangular cross-section.

As shown in Fig. 2(a), the beam is described using the material coordinate X along its length, with $X = 0$ at the bottom edge and $X = L$ at the top edge. The functions $x(X)$ and $z(X)$ denote the vertical and horizontal positions of a generic material point after deformation. The angle $\theta(X)$ represents the angle between the tangent to the beam at coordinate X and the vertical axis.

To cast Euler–Bernoulli's equation for the beam, we replace the constraint at the beam top edge with a pair of reaction forces, F_r and F_u in the horizontal and vertical directions respectively, and a reaction torque M_r. The internal bending moment $M(X)$ in a generic cross-section can thus be written as:

$$M(X) = M_r - F_r\,(x(L) - x(X)) - F_u\,(z(L) - z(X)). \qquad (1)$$

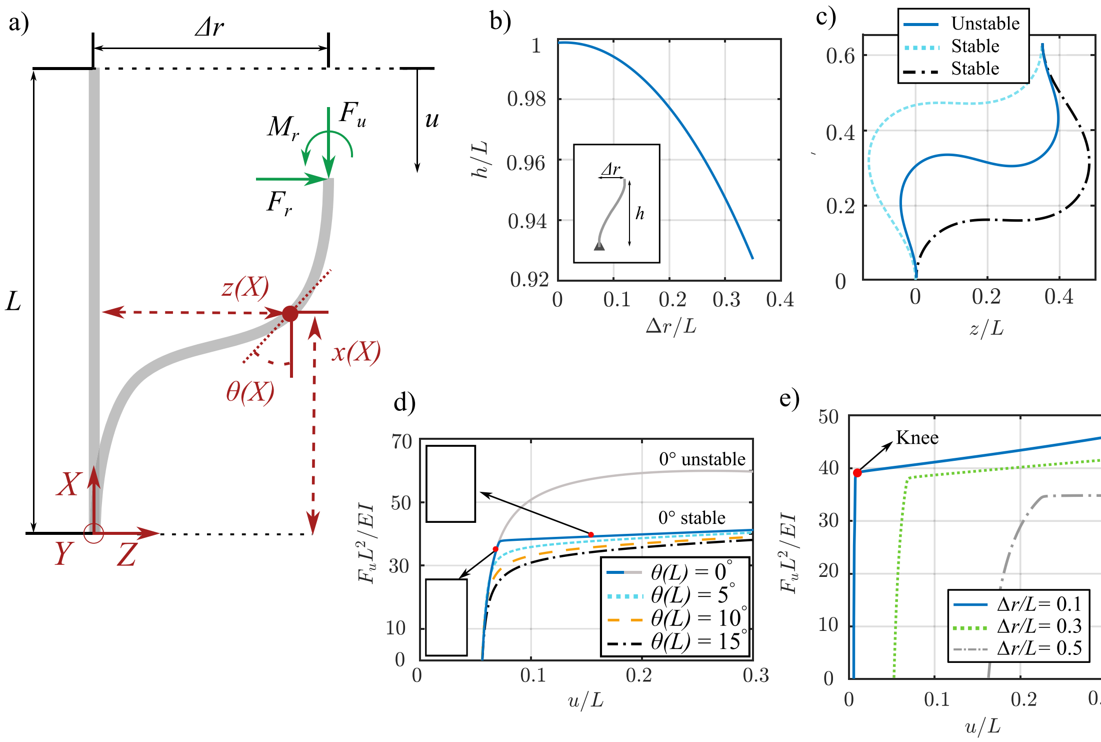

Fig. 2. (a) Schematic of a deformed beam of length L subjected to horizontal and vertical forces. The variables x, z, and θ denote the kinematic quantities expressed as functions of the material coordinate X. **(b)** Normalized beam height during horizontal preloading Δr. **(c)** Equilibrium shapes of the deformed beam under horizontal and vertical displacements, with $\theta(0) = \theta(L) = 0$. **(d)** Normalized vertical force F_u of a single beam as a function of the vertical displacement u for different mounting angles $\theta(L) = \theta_2$. **(e)** Normalized vertical force F_u for a single beam at different values of preloading Δr. The curves exhibit a plateau corresponding to the quasi-zero-stiffness region. The point where the curve exhibits a sharp change in slope is referred to as "knee".

According to Euler–Bernoulli's theory, the bending moment is related to the curvature as:

$$EI\,\frac{\mathrm{d}\theta}{\mathrm{d}X} = -M(X) = -M_r + F_r\,(x(L) - x(X)) + F_u\,(z(L) - z(X)). \tag{2}$$

where E is the beam's material Young's modulus, and I is the beam area moment of inertia.

Differentiating Eq. (2) with respect to X and using the kinematic relations, we obtain the following system of equations:

$$\begin{cases} EI\,\dfrac{\mathrm{d}^2\theta}{\mathrm{d}X^2} = -F_r\,\cos\theta - F_u\,\sin\theta, \\ \dfrac{\mathrm{d}x}{\mathrm{d}X} = \cos\theta, \\ \dfrac{\mathrm{d}z}{\mathrm{d}X} = \sin\theta, \end{cases} \tag{3}$$

Eq. (3) requires a set of boundary conditions to be solved, and is therefore formulated as a boundary value problem (BVP). To describe the beam shape variation during the preloading phase (when the beam is transversely pre–bent and mounted on the rigid frames, with no vertical force applied $F_u = 0$), the following boundary conditions are used:

$$\begin{cases} x(0) = 0, \quad z(0) = 0, \quad \theta(0) = \theta_1 \\ x(L) = \Delta r, \quad \theta(L) = \theta_2 \end{cases} \tag{4}$$

where θ_1, θ_2 are mounting angles at the beam edges and Δr is the horizontal preload. In the case of ideal mounting, $\theta_1 = \theta_2 = 0$. In practice, however, the beam exhibits a finite mounting angle at its ends due to assembly inaccuracies.

We solved system (3) numerically, using Matlab's built-in command *bvp4c*, treating θ, x and z as unknown functions and F_r and F_u as unknown parameters, fully determined by the boundary conditions. Alternative solution approaches are available, leading to analytical or semi-analytical solutions based on the elliptic integral solution [28,47].

Fig. 2(b) describes the beam kinematics during preloading. The plot reports the longitudinal (normalized) length h of a beam (after contraction due to bending - see Fig. 1a) as a function of the horizontal preload Δr, obtained by solving system (3) with boundary conditions (4), under the assumption that $F_u = 0$ (and u is thus unknown and depends on Δr). This result allows determining the longitudinal length h of the mechanism in mounting configurations, which decreases as Δr increases (leading to larger curvature equilibrium shapes). It is worth noting that the result of Fig. 2(b) holds true regardless of the material properties and the geometrical proportions of the beam (provided that the beam thickness is much smaller than its length), and it represents a purely kinematic result. Prescribing a transverse displacement Δr equal to 30% of the beam's initial length leads to a modest reduction of 6% in the longitudinal beam length.

Once the beam has been preloaded horizontally by Δr, the coupling with the EBM and its subsequent contraction imposes a vertical deformation. We therefore investigate the equilibrium shapes of the beam by considering an imposed vertical displacement $z(L) = u$, solving Eq. (3) with the following set of boundary conditions:

$$\begin{cases} x(0) = 0, \quad z(0) = 0, \quad \theta(0) = \theta_1, \\ x(L) = \Delta r, \quad z(L) = u, \quad \theta(L) = \theta_2. \end{cases} \tag{5}$$

u denotes a longitudinal displacement of the beam top end with respect to the undeformed straight configuration. Fig. 2(c) reports the beam shapes obtained by solving Eq. (3) with the boundary conditions in Eq. (5), assuming $\Delta r/L = 0.35$ and $u/L = 0.375$. For a reference case with zero mounting angles, i.e., $\theta(0) = \theta(L) = 0$, three equilibrium configurations are found, of which two are stable and one is unstable. The unstable deformed shape is symmetrical (i.e., it remains unchanged upon a double horizontal + vertical flipping around the beam mid-point), whereas the two stable positions are asymmetrical. Although all solutions are obtained numerically, in practice the beam is expected to adopt only the configurations corresponding to minimum potential energy, i.e., the stable ones. In practical scenarios, the stable configuration that is preferred by the system is determined by the inclination angle at the mounting edge.

In Fig. 2(d)–(e), we investigate the influence of boundary conditions on the normalized vertical force component $F_u L^2/(EI)$ during vertical deformation, considering only stable solutions. In Fig. 2(d), a non-zero rotation at the top end of the beam is introduced, i.e., $\theta(L) = \theta_2$. Due to the adopted mounting procedure (see Fig. 1b), the bottom end is fixed first, while the top edge is constrained after the beam has been prebent. As a result, a non-zero mounting angle is expected at the top edge, whereas it is reasonable to assume an ideal clamped condition at the bottom end, i.e., $\theta(0) = 0$.

The plot shows the force–displacement response for different mounting angles $\theta(L) = \theta_2$. For small compressive displacements, the beam follows a stable deformation pattern characterized by symmetric shapes. In this regime, the force increases sharply with u. For larger values of u, symmetric configurations become unstable, and the beam transitions to deformation patterns similar to those shown in Fig. 2(c). The vertical equilibrium force along these stable trajectories is lower than the force that would be required to enforce symmetric (unstable) bending configurations. Along the stable trajectories, the beam force response exhibits a plateau corresponding to a quasi-zero-stiffness (QZS) region, with a force value that is only weakly affected by the mounting angles. This represents a key advantage of the mechanism, as its response is robust to geometric imperfections such as inaccuracies in the mounting angles.

Fig. 2(e) reports the normalized force–displacement response obtained by varying a more controllable design parameter, namely the horizontal preload Δr. The simulations show that the force at the knee of the plateau (the point of the curve where the slope exhibits a sharp change) is mildly affected by this parameter, whereas the stiffness associated with the plateau strongly depends on it. In particular, the mechanism exhibits a more pronounced quasi-zero-stiffness behavior for larger preload values.

It should be noted that, owing to the low bending stiffness of the proposed mechanism, the contribution of axial compression to the overall deformation is negligible compared to that induced by beam bending. To corroborate this assumption, we consider the case of a dimensionless load $F_u L^2/(EI) \simeq 30$, which, according to Fig. 2(d), corresponds to a normalized displacement u/L on the order of 10^{-1}. For a flat beam, the axial compressive displacement due to a compressive force can be estimated as $u = F_u L/(EA)$, where A is the beam cross-sectional area. Using the previous assumption on the force value leads to a dimensionless compressive displacement $u/L = 30I/(L^2 A)$. For the geometry considered in this work (beam with rectangular cross-section), u/L is on the order of 10^{-4}, i.e., three orders of magnitude smaller than the displacement induced by bending.

3.2. Design guidelines

Here, we discuss trade-offs and outline possible strategies for the design of a QZS mechanism coupled with a target actuator. The objectives for the mechanism design are to provide the EBM with the ability to produce a target free stroke, and to restrain its extension in the presence of high externally applied forces.

Let us consider a given EBM device with a known response, described by a set of force–displacement curves (describing the actuator elastic response, and its response at constant voltage), as qualitatively shown in Fig. 3 (using the same graphical formalism as in Fig. 1d). The intersection between the elastic EBM force–displacement curve (black curves in Fig. 3) and the force–displacement response of the biasing mechanism (green curves) identifies the EBM equilibrium position. The intersection between the mechanism response and the EBM response at a given voltage (red dash-dot curves) identifies the zipped position of the device and, consequently, its free stroke.

A first key design choice consists in the definition of a target value for the QZS mechanism's plateau force. Such a value represents a trade-off: on the one hand, large mechanism preload forces reduce the useful actuator force output (as part of the generated electrostatic force is used to overcome the preload force, rather than producing work against an external load); on the other hand, low biasing forces result in small free displacements (Fig. 3a). The parameters governing the force response can be tuned to position the plateau at a desired level (see Section 3.1). According to Eq. (2), for a given length L of the beams, the mechanism force F_u scales proportionally with E and I (and therefore with the beam width b and the cube of the thickness t^3), and the number of beams. For a given choice of the material film (t and E fixed), the beam width b and the number of beams in the mechanism represent the main design parameters through which the force plateau value can be set.

The beams' length L and the radial offset Δr directly affect the mutual position of the equilibrium point (intersection between the EBM and the mechanism elastic responses), and the position of the knee in the mechanism force response. Fixing L and increasing Δr moves the knee point in the mechanism curve towards the left in the representation of Fig. 3(b), while weakly affecting the position of the equilibrium point (as the value of the plateau force depends weakly on $\Delta r/L$, as observed in Fig. 2e). A desirable feature for the coupled actuator–mechanism system is that the knee point falls close to (or in correspondence with) the coupled system's equilibrium point. If this is the case, applying an external force causes a limited additional extension of the EBM (on top of the EBM preloading), due to the mechanism tensile stiffness. This result can be achieved by using different combinations of L and Δr. The choice of the ratio $\Delta r/L$ comes from a trade-off: low values of $\Delta r/L$ (i.e., using vertical beams) lead to a high stiffness of the mechanism outside of the QZS region, but make the mechanism response depart from a QZS behavior (see Fig. 3(c)).

The theoretical framework and design considerations outlined so far were used to design a QZS mechanism to be coupled with a 3-unit EBM stack. From previous studies [11], it is known that stacks of 3 EBM units

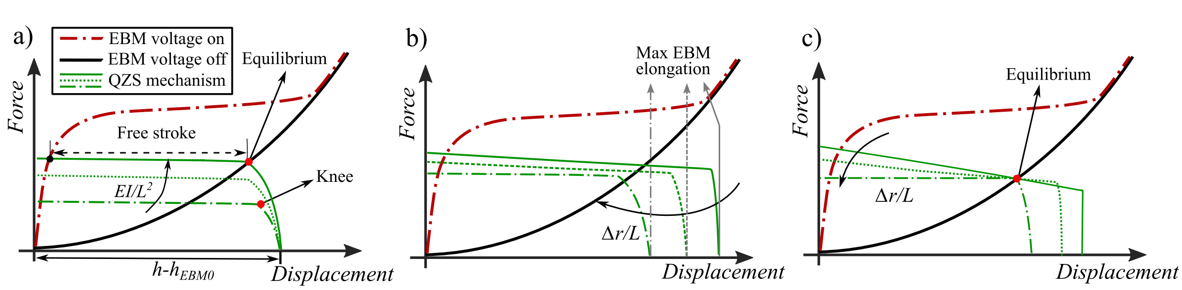

Fig. 3. Qualitative map of the influence of the design parameters on the response of a coupled EBM-QZS mechanism system. **(a)** The position of the force plateau of the mechanism affects the free stroke and the useful actuator force output. **(b)** The offset displacement Δr for a fixed beam length L affects the displacement beyond the equilibrium point, which may lead to overstretching. **(c)** For a chosen equilibrium point, the ratio $\Delta r/L$ influences the stiffness characteristics of the mechanism.

(with the target dimensions used in this work) can achieve strokes on the order of 4 mm under a minimum preload of 1 N. These values provided a reference for the initial design of the mechanism dimensions, which were subsequently refined based on experimental data.

4. Experimental setup and procedures

This section presents the procedures used to fabricate the tested EBM and QZS mechanism prototypes, and the experimental setups developed to characterize the response of the individual components and the coupled actuator-mechanism system.

4.1. Materials and manufacturing

The manufactured EBM prototype is a stack made of 3 units (dimensions as in [11], with an outer electrode diameter of 30 mm) with a reservoir mechanically connected in series and manufactured using a procedure similar to that described in [11]. Each unit consists of two dielectric polyimide (PI) films (PIT1N by CAPLINQ - 25 µm thickness), connected along a circular perimeter with a double-sided annular adhesive tape (Nitto 5600 - 5 µm), and secured externally by two rigid annular frames (inner diameter 30 mm, outer diameter 40 mm). The annular frames were obtained from FR-4 epoxy resin sheets (0.3 mm thickness) and attached to the polyimide film substrates via 0.1 mm double-sided acrylic adhesive tape (68144, Tesa). Double-sided adhesive pads (VHB 4905 by 3M; outer diameter 15 mm) on the external surfaces were used to bond adjacent units or interface elements. An annular region on the dielectric film's outer surface, between the rigid frames and the connecting pads, was painted with carbon paint (Ted Pella DAG-T-502) to form compliant electrodes. The rigid interface end-effector was 3D-printed (Black resin V5, Formlabs). Small coaxial holes (5 mm diameter) in the polyimide layers allow dielectric fluid to flow through the units and the reservoir during pouch zipping and unzipping.

The reservoir holds dielectric fluid (silicone oil-PMX 200 - 50 cSt) within a flexible VHB tape wall, which allows volume variation during operation. An annular 3D–printed rigid frame constrains and bonds the VHB tape to a PI film layer that serves as the reservoir top lid. A concentric internal cylindrical manifold (7 mm height; outer diameter 15 mm), made from PLA (PLA Basic by Bambulab), drives the oil-flow pattern between the VHB tape and the top PI film, creating a conical reservoir shape.

The QZS mechanism features three beams arranged circumferentially on two rigid frames (60 mm top frame diameter, corresponding to the outer diameter of the reservoir, and 47 mm bottom frame diameter). In the case of the QZS mounted with the EBM, the 3D–printed rigid frame that creates the reservoir perimeter is used as the top frame of the QZS mechanism. The beams (3 mm in width, 20 mm of active length and 0.125 mm in thickness) are laser-cut from a BoPET sheet (Mylar-A-125-091 by DuPont; 125 µm thick). To assemble the mechanism, the top ends of the beams were first inserted into slits on the top rigid frame and glued while maintaining a vertical position. The bottom ends of the beams were then inserted and secured (with glue) into slits present on a bottom frame (connected to the device end-effector), which resulted in a horizontal displacement $\Delta r = 7$ mm and thus bending. The clearance between the beams and the slits allows the beams to adopt a non–zero inclination angle. Testing on different replicas of the mechanism showed that this angle (as well as the force-stroke response of the mechanism) is repeatable. It should be noted that the presented manufacturing process is intended for rapid prototyping and proof-of-concept validation. The manufacturing procedures used here present significant margins for improvement, including the design of the mechanism structural frames, beam connections, and EBM reservoir implementation, which would enhance the system's scalability, robustness, and long-term reliability.

The active mass of the empty 3-unit EBM stack (including the weight of the reservoir and the structural elements, excluding the end effector used to connect the device to the test-bench) is 9.2 g. The EBM is filled with 7.4 ml of silicone oil, resulting in a total mass of 16.6 g. Integrating the QZS mechanism, which consists of one additional bottom rigid plate (used to secure the beams' bottom ends) and the three beams, adds a mass of 1.5 g (almost entirely due to the additional rigid elements, since the weight of the beams alone is on the order of 0.03 g). Based on their materials and dimensions, the beams are expected to experience resonance in the first structural bending mode at a natural frequency on the order of 50 Hz, estimated using established relationships for straight clamped–clamped beams [48]. Although this represents only an approximate estimate (since the beams in the proposed mechanism are pre-bent), it provides an order-of-magnitude indication of the maximum frequency range in which the system can operate without incurring higher-order dynamical effects. The typical expected frequency range for the EBM actuator is on the order of a few Hertz [11], i.e., well below the expected natural frequency of the beams' bending mode.

4.2. Experimental setup and procedures

Experiments were conducted using the customized test bench shown in Fig. 4. A linear motor (Actuonix L16-100-150-12-P) is mounted on the top side of a rigid frame (made of metal struts) and connected to the EBM system via a long silicone band (Dragon Skin 20NV) to transmit force. A load cell (ME KD24s-5 N), attached to the bottom end of the EBM, is used to measure the applied force. A precision laser displacement sensor (optoNCDT 1320-25) is installed on the frame to measure displacements during testing. A real-time target machine (Speedgoat Performance Target, 3.1 GHz, equipped with an IO131 16-bit module) is used for data acquisition and control. Low-voltage signals from the real-time system drive a high-voltage amplifier (UltraVolt HVA series, 15 kV, 1.5 W), which supplies the EBM. The amplifier's built-in voltage monitor is used to measure the output voltage during the tests.

The experimental campaign includes both static and dynamic tests. Static tests are performed on the QZS mechanism alone, the EBM alone, and the coupled system.

In the static tests, the objective is to extract the force–displacement response of the actuator or the mechanism. For the QZS mechanism, the structure is fixed through its bottom rigid ring and aligned coaxially with the linear motor. The load cell is mounted on the actuator head

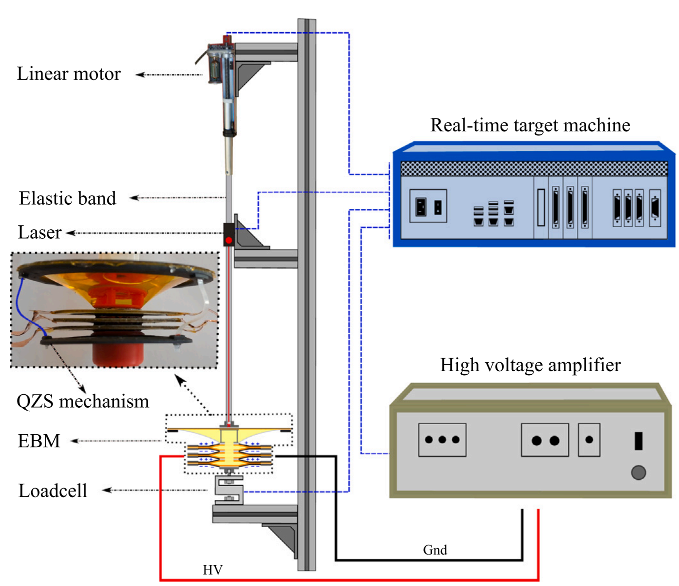

Fig. 4. Schematic of the experimental test bench used for static and dynamic characterization. A real-time control system is employed for data acquisition and control, driving a position-controlled linear motor and applying voltage profiles through a high-voltage (HV) amplifier. A force is applied via a long, slender spring, with the force measured by a load cell. Displacements are measured using a laser sensor.

via rigid connectors. By controlling the motor position, the mechanism is compressed, while the load cell and the laser sensor simultaneously measure force and displacement throughout the test.

For the static tests performed on both the EBM and the coupled system, the load cell is mounted at the bottom of the rigid support, as shown in Fig. 4. In these tests, a high-voltage signal is first applied to the EBM system, after which the linear motor is driven in position control mode. The voltage profile consists of a square wave with active pulses of 1 s followed by resting phases of 5 s to guarantee complete actuator return to the unzipped position (following a procedure similar to that used in [10]). The polarity of the voltage is reversed at each pulse to counteract charge accumulation [49]. During actuation, the linear motor simultaneously moves downward, pulling the device through a compliant silicone band connected at the top. The band's large length and low stiffness ensure that force variations due to the small EBM contractions during each actuation cycle are minimal (compared to the elastic bias force), as observed in previous studies [12,49]. The continuous position control of the motor results in a gradual increase in the applied force over time.

Dynamic tests were performed on both the EBM alone and the coupled system. To ensure a constant applied force, the linear motor (connected to the elastic band) was position-controlled to a fixed location and held throughout the duration of the experiment. The EBM was driven by square voltage pulses with increasing frequency and a duty cycle of 50%, resulting in actuation frequencies ranging from 0.5 Hz to 10 Hz.

In all tests, force and displacement data were acquired at a sampling rate of 10 kHz.

5. Experimental results

This section presents an experimental proof of concept for the proposed coupled EBM–QZS mechanism coupled system. First, an experimental validation of the QZS mechanism model from Section 3 is presented. Secondly, results of static and dynamic tests on the EBM with the QZS structure are reported and compared to the baseline performance of an EBM without the QZS mechanism.

5.1. Beam model validation

The analytical model presented in Section 3 is here validated experimentally. First, the profile of the beams during deformation is compared with model predictions (Fig. 5a). Compression tests are carried out on an experimental prototype of the QZS mechanism (as in Fig. 1b) made of 3 beams, each with the same geometrical dimensions: $L = 20\,\mathrm{mm}$, $t = 0.125\,\mathrm{mm}$, $b = 3\,\mathrm{mm}$. Images of the beam are captured during deformation using a camera (AOS PromonU1000) and compared with the analytical predictions (Fig. 5a). After mounting, the top edge is fixed at a horizontal offset of $\Delta r = 7\,\mathrm{mm}$ (left image). A vertical displacement corresponding to $L - h - u$ is then imposed in steps of 2 mm (central and right images) by means of a position-controlled motor. Because the ends of the beams are attached to the rigid frames through a slit with finite thickness (larger than the beam thickness) after preloading, the mounting angle θ_2 (as defined in Section 3) is expected to be different from zero. The mounting angle is identified from the left snapshot of Fig. 5(a) by superimposing the predicted beam shape onto the experimental profile and by tuning the value until matching with the camera–recorded profile is reached. A value of $\theta(L) = \theta_2 = 8°$ is obtained and subsequently used for all shape and force predictions during vertical deformation. This value of θ_2 closely matches the angle between the vertical height and the horizontal thickness of the slit within which the beam is mounted, confirming that the source of this mounting angle is geometrical. The difference in thickness between the beam and the slit opening that generates this angle is difficult to avoid (as the mounting frames are produced by additive manufacturing), but it is repeatable throughout different replicas of the mechanism. With this initial calibration, the model accurately captures the beam deformed shapes.

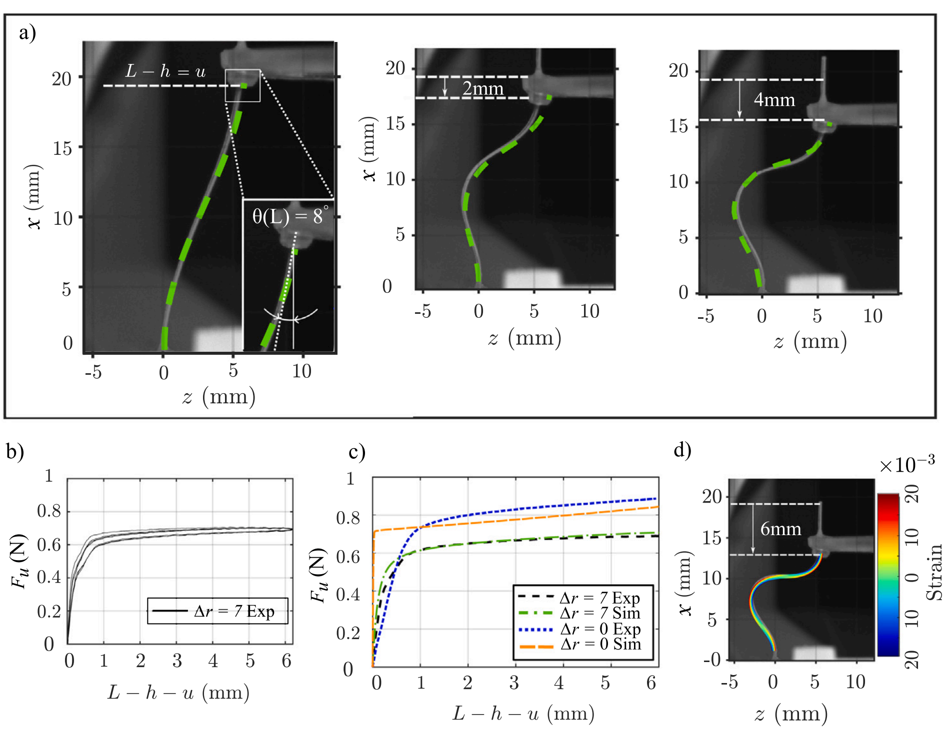

Fig. 5. (a) Comparison between experimentally captured beam shapes and model predictions. The left image highlights the presence of a mounting angle, identified as $\theta(L) = 8°$. Assuming a constant value of $\theta(L)$, the central and right images show good agreement between experiments and model predictions under vertical deformation. **(b)** Cyclic compressive response of a mechanism with $\Delta r = 7\,\mathrm{mm}$ over 5 cycles. **(c)** Validation of the simulated force response for two realisations of the QZS mechanism having $\Delta r = 0$ and $\Delta r = 7\,\mathrm{mm}$. The experimental results represent average force-displacement curves (averaged over forward and return strokes). **(d)** Estimated strain distribution along the beam under a worst-case vertical deformation. The maximum strain is less than 2%.

The result of a cyclic compression test on the QZS mechanism with $\Delta r = 7$ mm is shown in Fig. 5(b). The response of the QZS mechanism stabilizes and becomes repeatable (across different cycles) after the first cycle, and the QZS plateau stabilizes around 0.7 N. The difference between the loading and unloading curves of the QZS mechanism indicates a limited hysteresis, corresponding to 5.8%, calculated as the ratio of dissipated energy to stored elastic energy.

Fig. 5(c) presents a comparison of experimental and simulated force–displacement responses of the full mechanism. Experimental data are obtained by averaging the force–displacement response of the QZS mechanism over a full stabilized cycle (forward + return stroke). Simulations are performed assuming a Young's modulus $E = 5$ GPa, experimentally measured through a tensile test on a dog-bone Mylar specimen according to ISO 527–2 1BA. The response of the full mechanism is obtained by scaling the force–displacement curve of a single beam by a factor of three. The force-displacement model prediction is validated against two configurations of the QZS mechanism, namely, the above–mentioned reference configuration with $\Delta r = 7$ mm, and a configuration with straight vertical beams ($\Delta r = 0$ mm). In the case with $\Delta r = 0$, since no bending is applied to the beams during installation, the mounting angles at both edges are assumed to be 0 ($\theta(0) = \theta(L) = 0$). The experimental curves corresponding to these two cases exhibit distinct behaviors. The reference configuration ($\Delta r = 7$ mm) exhibits a response that mildly transitions from an initial high-stiffness response to a force plateau, close to a QZS behavior. In contrast to that, and consistently with the theoretical predictions, in the absence of horizontal preload ($\Delta r = 0$), the force plateau further departs from a QZS response, showing a positive–slope trend. In this latter case, the predicted force-displacement behavior shows an initial steep increase in force (followed by a low-stiffness region after buckling), while the experimental trend shows that the force follows a gradual increase. This happens because the configuration with vertical beams is highly sensitive to misalignments (e.g., angles between the direction of force application and the beams axis) or slight differences in the beams' length, which cause the different beams not to buckle simultaneously. In general, using a horizontal preload Δr makes the mechanism response more easily predictable and robust against mounting tolerances. The comparison between the model and experimental results demonstrates good agreement, with the $\Delta r = 7$ mm case exhibiting a strong overlap between the predicted and measured responses. In contrast, for $\Delta r = 0$ mm, a significant discrepancy is observed in the region preceding the knee, due to the above mentioned non-simultaneous buckling of the three beams.

In Fig. 5(d), we evaluate the strain distribution along the preloaded beam in correspondence with a vertical deformation of 6 mm. This represents a worst–case scenario, considering the working conditions of the mechanism in combination with a 3-unit EBM. The strain is a consequence of the beam kinematics and is independent of the material properties. The maximum strain is applied on the outer fibers of the beam, located at distances $\pm t/2$ from the neutral axis, where t is the beam thickness. The strains ε in the top and bottom fibers are given by:

$$\varepsilon = \pm \frac{t}{2}\,\frac{d\theta}{dX}, \tag{6}$$

The maximum strain is reached in the sections with maximum curvature, and it reaches maximum values below 2%, within reported working limits for Mylar [50].

5.2. Performance of the EBM with QZS biasing mechanism

We performed a characterization of an EBM prototype coupled with a QZS mechanism (with preloaded beams) described in Section 5.1, and compared it with the baseline performance of an EBM with no coupled biasing element (Fig. 6).

Fig. 6(a)–(b) report the results of quasi-static tests, in which a slowly varying force is applied while the system displacement is monitored under cyclic voltage activation. The figures compare the behavior of the EBM alone and when coupled with the QZS mechanism, respectively. The actuator displacement (as defined in the plots) corresponds to the motion of the top edge of the device (connected to the elastic band) with respect to the mounting configuration, and it increases progressively with the applied external force. Applying voltage pulses (here with an amplitude of 5 kV) induces cyclic actuation of the device. During each cycle, the EBM exhibits a local maximum (unzipped state) and a local minimum (zipped state), with the difference between these values defining the stroke.

From the displacement response in Fig. 6(a), it can be observed that, in the absence of a biasing mechanism, the EBM exhibits zero stroke until a preload threshold is reached (approximately 0.5 N), below which it remains fully zipped. Beyond this point, the stack begins to open and, upon voltage actuation, a finite stroke is obtained, reaching a local maximum. The lack of stroke below a certain force threshold may be attributed to residual charges during the initial activation cycles [49], or to mechanical locking effects occurring in the absence of a restoring force, which can lead to complete evacuation of the fluid gap and stiction between the dielectric layers. This limitation is not observed in the configuration incorporating the QZS mechanism, where the elastic response of the mechanism enables re-opening of the EBM after each actuation cycle. As shown in Fig. 6(b), a finite stroke is obtained even in the absence of an external load. The EBM coupled with the QZS mechanism exhibits its maximum stroke at zero applied force. As the externally applied force increases, the stroke decreases.

From Figs. 6(a) and 5(b), we can reconstruct an experimental equivalent of the force–displacement curves reported in Fig. 1(d), obtaining the result shown in Fig. 6(c). Specifically, from Fig. 6(a), we extract the envelope of the local maxima (elastic response) and the envelope of the local minima (response at constant voltage, here 5 kV) of the displacement time history. These envelopes correspond to the elastic response of the EBM (no applied voltage) and the response under constant voltage, respectively, and are represented as the black solid and red dashed curves in Fig. 6(c). Similar to Fig. 1(d), these two curves are intersected with the curve representing the QZS response (purple), which is the same as identified in the experiment reported in Fig. 5(b) (configuration with $\Delta r = 7$ mm). According to the data in Fig. 6(c), the average stiffness of the passive EBM in the range 0–6 mm is on the order of 170 N/m, whereas the QZS mechanism stiffness in the plateau region is lower than 15 N/m. In working conditions, the stiffness of the coupled system is thus largely dominated by the EBM, with the QZS mechanism serving as a source of constant bias force. The intersection points of the QZS response with the EBM response (at 0 and 5 kV) suggest an expected stroke on the order of ~ 4 mm.

To study the effect of external forces on the EBM elongation, a uniaxial tensile test is performed on both the EBM and the coupled EBM–QZS system. The passive elongation (i.e., with no voltage applied) of the two configurations is reported in Fig. 6(d), where zero elongation corresponds to the flat (fully zipped) configuration of the EBM. When a tensile force is applied to the bare EBM, a steep increase in elongation is observed, indicating low tensile stiffness. In contrast, when the same force is applied to the coupled EBM–QZS system, only a modest additional elongation is measured beyond the initial preloaded configuration. This behavior is attributed to the progressive tensioning of the beams, which increasingly bear the applied external force, thereby limiting the extension of the EBM. This behavior is further illustrated in Fig. 6(e), which demonstrates the ability of the QZS mechanism to prevent overstretching of the EBM. In the experiment, a mass of 700 g is suspended from both the bare EBM and the coupled system. While the standalone EBM undergoes significant elongation (on the order of 14.5 mm), ultimately leading to permanent deformation (e.g., creep of the adhesive layers connecting the units), the coupled system withstands the same load without damage. In this case, the beams approach a nearly straight configuration (corresponding to an elongation of the EBM of ~ 7 mm). In this configuration, they provide a strong resistance to further elongation, thereby significantly increasing the tensile stiffness of the system

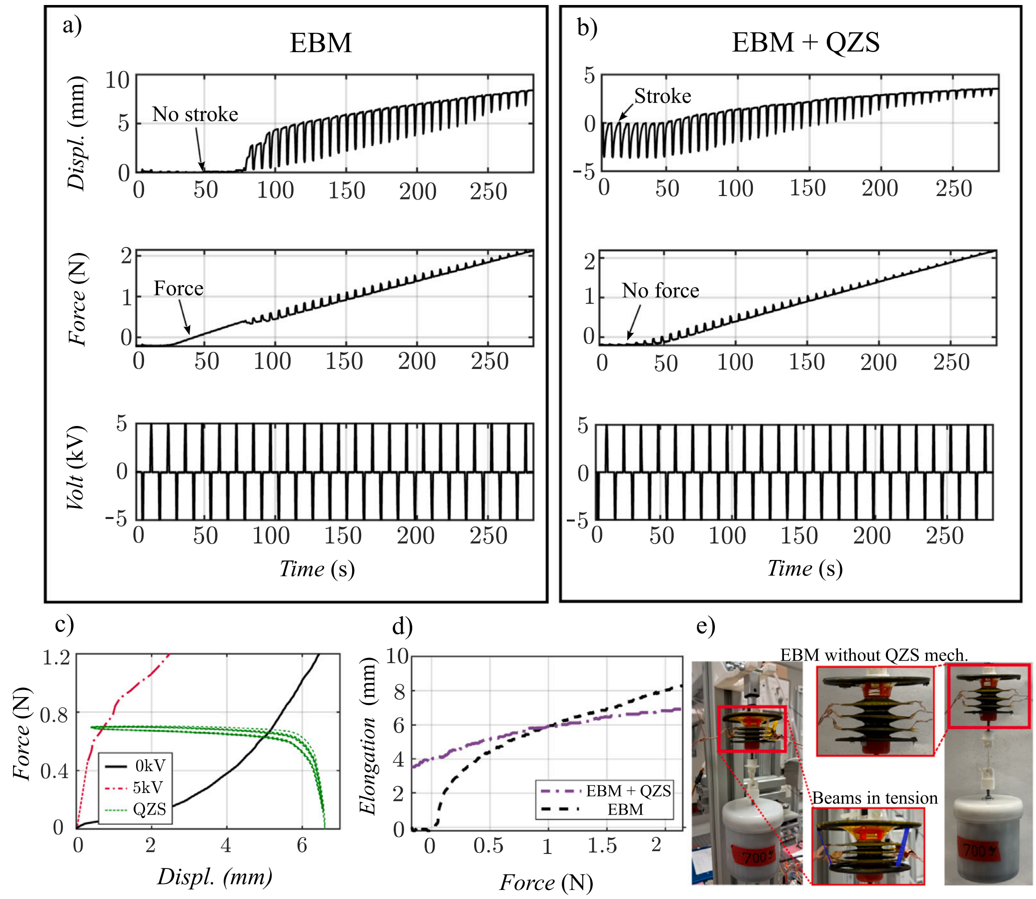

Fig. 6. Characterization of the force–displacement–voltage response of the EBM **(a)**, and the EBM with QZS mechanism **(b)**. The displacement (top plot) is measured by gradually loading the device through a spring (central plot), while closure is achieved by applying a high-voltage (HV) signal (bottom plot). **(c)** Experimental representation of the force-displacement curves of the EBM obtained by interpolating the upper and lower peaks of the displacement signal. The intersection with the QZS mechanism provides a quantitative estimate of the expected stroke of the integrated system. **(d)** Tensile test of the EBM and the coupled EBM–QZS system. Beam tensioning strongly limits the elongation. **(e)** Visual demonstration that the QZS mechanism prevents overstretching of the EBM under large external loads.

in case of overloads, and protecting the EBM from excessive deformation (e.g., straining of the dielectric films and the connecting adhesive layers). To quantify the tensile stiffness of the mechanism in comparison to the EBM tensile stiffness, we performed a tensile test on the QZS mechanism on a universal tensile testing machine (Instron 5060, position-controlled with an elongation rate of 1 mm/min). From the measured force and displacement under tensile loads, we measured a tensile stiffness of 11 N/mm for the QZS mechanism (tens of times higher than the EBM tensile stiffness, on the order of 170 N/m). Such a stiffness is associated with a bending deformation of the structural frames of the mechanism (rather than to elongation of the beams), and could be further increased by leveraging the frames' materials and design. In our tensile experiments, the mechanism could withstand tensile forces of several tens of Newtons, again, limited by rupture of the structural frames.

Fig. 7(a) provides a comparison of the quasi-static stroke-force relationship of the 3-unit EBM with and without the QZS mechanism under an actuation voltage of 5 kV. The computation of the stroke curve is derived from the difference between the experimental displacement envelopes of local minima and maxima, as reported for the EBM case in Fig. 6(c). The stroke response of the EBM–QZS structure and that of the sole EBM follow similar trends (with the stroke decreasing as a function of the load) but they are shifted apart along the force axis (the bare EBM reaches larger strokes at larger loads, but no stroke at low forces). The horizontal offset is roughly equal to the plateau value of the force of the QZS mechanism ($\sim 0.7\,\mathrm{N}$). This occurs because the QZS mechanism applies a nearly constant additional load on the EBM (in addition to the external load). While this allows the actuator to provide a stroke at low loads, it reduces the useful force the actuator can produce by an amount equal to the preload itself. The maximum stroke of the EBM without QZS (at $\sim 0.8\,\mathrm{N}$) is higher than that of the EBM with QZS (at $\sim 0.2\,\mathrm{N}$) by approximately 10%, because the beams constrain the EBM elongation in the presence of tensile forces. The maximum stroke of the integrated system is a result of the QZS mechanism design, which must achieve a trade-off among maximum stroke, safe stretching limit, and output force reduction due to preloading, as discussed in Section 3.2.

In Fig. 7(b) we investigate the effect of different applied voltages on the coupled EBM–QZS mechanism system. As expected, the stroke at a given force increases with the applied voltage. Lower voltages (3 kV) lead to no actuation (blocking) in the presence of larger forces. For external forces close to zero, applying 5 or 7 kV leads to similar strokes, as both voltages are sufficient to fully zip the device. For a higher voltage of 7 kV, the maximum stroke (4.51 mm) is reached in the presence of an applied force of approximately 0.7 N (rather than at 0 N). This happens because the external force causes an additional (yet limited) extension of the combined EBM–QZS system. The maximum stroke of the EBM corresponds to a contraction of 21.5% with respect to the EBM equilibrium length (including reservoir and frame height), and an actuation energy density of 0.33 J/kg. While for the purpose of this work no measures were taken to optimise the EBM design (e.g., reduce the frame or the reservoir thickness and mass), these results are still comparable with those obtained in [11].

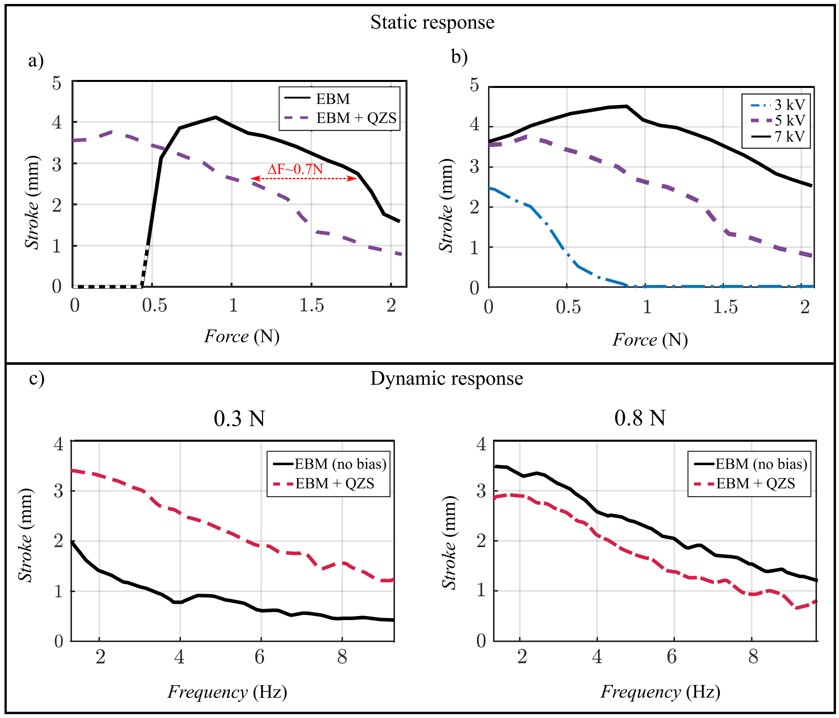

Fig. 7. (a) Quasi-static stroke–force experimental curves at a constant applied voltage of 5 kV for a 3-unit EBM and the coupled EBM–QZS mechanism. **(b)** Effect of the applied voltage on the quasi–static stroke–force curves (coupled system). **(c)** Dynamic response of a 3-unit EBM under a frequency sweep at 5 kV and different applied forces (0.3 and 0.8 N): comparison of unbiased EBM and EBM with QZS mechanism.

To evaluate the impact of the QZS mechanism on the system dynamics, we performed actuation tests by sweeping the excitation frequency from 0.5 to 10 Hz, over a time window of 50 s, under constant external loads of 0.3 and 0.8 N and a voltage of 5 kV (see Supplementary Video). As shown in Fig. 7(c), the stroke amplitude decreases with increasing frequency for both configurations (with and without the biasing element) because of the system dynamics. The differences in stroke at low frequency for the different forces are consistent with those reported in quasi-static tests (Fig. 7(a)–(b)): the biased EBM produces larger strokes at low loads (0.3 N), and lower strokes at higher loads (0.8 N), due to the additional preload of the mechanism. At a frequency of 10 Hz, the reduction in stroke is comparable for the EBM and the EBM–QZS mechanism, proving that the dynamics and the frequency response are governed by the EBM (especially by the dielectric fluid's mechanical dynamics), and the QZS mechanism does not compromise the frequency response. This is consistent with the observation that the mechanism hysteresis (Fig. 5b) is limited (below 10%).

6. Conclusions

This study investigates the design and coupling of a quasi-zero stiffness (QZS) mechanism as a biasing element for electrostatic zipping actuators, with particular reference to electrostatic bellow muscle (EBM) actuators. EBMs are zipping actuators featuring a deformable multi-layer liquid-polymer dielectric layout, which contract in response to an applied voltage. While lending themselves to stroke upscaling via stacking, a limitation of EBMs is that they require a minimum amount of preload to produce a stroke. We propose a QZS mechanism devised with the dual aim of providing the EBM with a preload, hence decoupling its maximum stroke from the externally applied forces, and protecting the device from overstretching. The QZS mechanism consists of three bending beams enveloping the EBM. Preloading of the EBM induces compression buckling of the beams, whose deformation accommodates a longitudinal compression. Voltage-induced zipping of the EBM leads to extra compression buckling of the beams, which respond with a nearly constant force that allows reopening the device after actuation, without adding stiffness that would otherwise reduce the actuator stroke.

We formulated an analytical model of the QZS mechanism based on the elastica beam formulation to describe the deformed beam profiles and the effect of the geometrical parameters on the force response during bending. Based on the model, we elaborated a set of guidelines to design QZS mechanisms matched to a target EBM device.

Based on those guidelines, we designed a biasing mechanism for a 3-unit EBM stack with a diameter of 30 mm and a stroke capability on the order of 4 mm. The additional mass of the beam elements is three orders of magnitude lower than the EBM mass, and additional structural elements used to accommodate the mechanism cause an increase of less than 10% in the actuator weight.

A set of experiments on the QZS mechanism prototype validated results from the analytical model in terms of beam deformed shapes and force-displacement response. We proved that, in the presence of applied external loads 40 times larger than the device weight, an EBM coupled with a QZS mechanism exhibits maximum elongations that are one half of those reached by the sole EBM, demonstrating the effectiveness of the mechanism as a safety feature in the presence of large loads. Actuation tests showed that an EBM coupled with a QZS mechanism (and no external load applied) can reach strokes comparable to the maximum strokes achieved by the bare EBM. The possibility of achieving strokes in the absence of external loads comes at the cost of a reduction in the output force capability of the actuator, since a fraction of the electrostatic force is required to overcome the preload force of the mechanism. Results from dynamic tests at different actuation frequencies showed that the QZS mechanism is not detrimental to the actuator frequency response, which is instead dominated by fluidic effects.

The proposed biasing mechanism features a design that is modular, and could be adapted to different embodiments of the EBM (e.g., stacks with a larger number of units) or to different zipping actuator concepts (e.g., electro-ribbons or honeycomb actuators). Future work will address optimised design procedures (e.g., optimised materials and design of the structural elements), and the study of the coupled actuator-QZS mechanism dynamics, to highlight the influence of the mechanism structural dynamics and nonlinear response on the global system response. Moreover, alternative materials and scalable manufacturing procedures will be investigated, with the aim not only of achieving target static and dynamic performance, but also of meeting target requirements in terms of cyclic and long-term device durability and lifetime.

CRediT authorship contribution statement

Hadi Taghvaei: Writing – original draft, Visualization, Validation, Investigation, Data curation. **Marco Riva:** Writing – original draft, Visualization, Software, Investigation, Formal analysis. **Matteo Benedetti:** Writing – review & editing, Supervision, Methodology. **Marco Fontana:** Writing – review & editing, Methodology, Conceptualization. **Pasquale Gallo:** Writing – review & editing, Supervision, Methodology, Conceptualization. **Giacomo Moretti:** Writing – review & editing, Supervision, Project administration, Methodology, Funding acquisition, Formal analysis, Conceptualization.

Funding

This research has been funded by European Union (EU) under the ERC Starting Grant project flEAP (GA: 101163668) and the Italian Ministry for University and Research (MUR) through the "Departments of Excellence 2023-27" program (L.232/2016) awarded to the Department of Industrial Engineering. The views and opinions expressed are however those of the authors only and do not necessarily reflect those of the EU, the ERC or the MUR. Neither the EU, the MUR nor the granting authorities can be held responsible for them.

Declaration of competing interest

The authors declare that they have no known competing financial interests or personal relationships that could have appeared to influence the work reported in this paper.

Acknowledgements

The authors would like to thank Mr. Massimo Emanuele De Cinque for the technical support provided during the tests. The authors are grateful to Nitto Denko Corporation (in particular, Mr. Paolo Bosso) for providing double sided adhesive tape used for prototype manufacturing.

Appendix A. Supplementary data

Supplementary data for this article can be found online at doi:10.1016/j.matdes.2026.116584.

Data availability

Data will be made available upon request.

References

[1] P. Rothemund, N. Kellaris, S.K. Mitchell, E. Acome, C. Keplinger, HASEL artificial muscles for a new generation of lifelike robots—recent progress and future opportunities, Adv. Mater. 33 (19) (2021) 2003375.
[2] N. Kellaris, V. Gopaluni Venkata, G.M. Smith, S.K. Mitchell, C. Keplinger, Peano-HASEL actuators: muscle-mimetic, electrohydraulic transducers that linearly contract on activation, Sci. Robot. 3 (14) (2018) eaar3276.
[3] S.-D. Gravert, E. Varini, A. Kazemipour, M.Y. Michelis, T. Buchner, R. Hinchet, R.K. Katzschmann, Low-voltage electrohydraulic actuators for untethered robotics, Sci. Adv. 10 (1) (2024) eadi9319.
[4] F. Hartmann, L. Penkner, D. Danninger, N. Arnold, M. Kaltenbrunner, Soft tunable lenses based on zipping electroactive polymer actuators, Adv. Sci. 8 (3) (2021) 2003104.
[5] E. Leroy, H. Shea, Hydraulically amplified electrostatic taxels (HAXELs) for full body haptics, Adv. Mater. Technol. 8 (16) (2023) 2300242.
[6] T.J. Buchner, T. Fukushima, A. Kazemipour, S.-D. Gravert, M. Prairie, P. Romanescu, P. Arm, Y. Zhang, X. Wang, S.L. Zhang, et al., Electrohydraulic musculoskeletal robotic leg for agile, adaptive, yet energy-efficient locomotion, Nat. Commun. 15 (1) (2024) 7634.
[7] G.M. Whitesides, Soft robotics, Angew. Chem. Int. Ed. 57 (2018) 4258–4273.
[8] G. Moretti, M. Duranti, M. Righi, R. Vertechy, M. Fontana, Analysis of dielectric fluid transducers, in: Electroactive Polymer Actuators and Devices (EAPAD) XX, vol. 10594, SPIE, 2018, pp. 142–154.
[9] M. Taghavi, T. Helps, J. Rossiter, Electro-ribbon actuators and electro-origami robots, Sci. Robot. 3 (25) (2018) eaau9795.
[10] F. Caruso, A. Firouzeh, H. Shea, Scalable high-force zipping electrostatic actuators, Adv. Intell. Syst. (2026) e202501315.
[11] I.-D. Sîrbu, G. Moretti, G. Bortolotti, M. Bolignari, S. Dirè, L. Fambri, R. Vertechy, M. Fontana, Electrostatic bellow muscle actuators and energy harvesters that stack up, Sci. Robot. 6 (51) (2021) eaaz5796.
[12] I.-D. Sîrbu, A. Mazzotta, U. Tosi, D. Bortoluzzi, V. Mattoli, G. Moretti, M. Fontana, Vacuum-gap electrostatic multilayer actuators for space robotics, Nat. Commun. 16 (2025) 11414.
[13] L.-C. Zhao, H.-X. Zou, K.-X. Wei, S.-X. Zhou, G. Meng, W.-M. Zhang, Mechanical intelligent energy harvesting: from methodology to applications, Adv. Energy Mater. 13 (29) (2023) 2300557.
[14] S. Hoh, T. Helps, R.S. Diteesawat, M. Taghavi, J. Rossiter, Electro-lattice actuator: a compliant high-contractile active lattice structure, Smart Mater. Struct. 30 (12) (2021) 125034.
[15] F. Royer, J.Z. Zhang, K. Overby, E.Y. Zhu, H. Bhundiya, J. Lang, Z.C. Cordero, Electrostatically actuated thin-shell space structures, in: AIAA SCITECH 2023 Forum, 2023, pp. 1302.
[16] N. Hou, J. Wen, Y. Pan, M. Taghavi, Origami-inspired modular electro-ribbon actuator for multi-degrees of freedom motion, Adv. Intell. Syst. 6 (6) (2024) 2300738.
[17] W. Sun, Y. Xu, M. Taghavi, A flexi-limbed electroactive frame for gripping and locomotion: structural optimization, Int. J. Mech. Sci. 286 (2025) 109862.
[18] J. Liu, Y. Zhao, H. Fu, Y. Liu, X. Zhou, An electro-ribbon actuator for robotic applications, J. Appl. Phys. 138 (16) (2025).
[19] W. Sun, J. Liu, Y. Xu, J. Li, M. Taghavi, Electroactive twisted ribbon for torsional zipping actuator, IEEE Robot. Autom. Lett. 10 (2025).
[20] E. Hajiesmaili, D.R. Clarke, Dielectric elastomer actuators, J. Appl. Phys. 129 (15) (2021).
[21] G. Berselli, R. Vertechy, G. Vassura, V. Parenti-Castelli, Optimal synthesis of conically shaped dielectric elastomer linear actuators: design methodology and experimental validation, IEEE/ASME Trans. Mechatron. 16 (1) (2011) 67–79.
[22] M. Hodgins, A. York, S. Seelecke, Experimental comparison of bias elements for out-of-plane DEAP actuator system, Smart Mater. Struct. 22 (9) (2013) 094016.
[23] S. Hau, D. Bruch, G. Rizzello, P. Motzki, S. Seelecke, Silicone based dielectric elastomer strip actuators coupled with nonlinear biasing elements for large actuation strains, Smart Mater. Struct. 27 (7) (2018) 074003.
[24] J. Neu, J. Hubertus, S. Croce, G. Schultes, S. Seelecke, G. Rizzello, Fully polymeric domes as high-stroke biasing system for soft dielectric elastomer actuators, Front. Robot. AI 8 (2021) 695918.
[25] S. Addario, A. Priuli, J. Hubertus, S. Gratz-Kelly, J. Neu, G. Schultes, S. Seelecke, G. Rizzello, Thermoplastic-polymer-based negative stiffness biasing mechanism for high stroke dielectric elastomer actuator systems, in: Electroactive Polymer Actuators and Devices (EAPAD) XXVI, vol. 12945, SPIE, 2024, pp. 79–90.
[26] H. Li, Y. Li, J. Li, Negative stiffness devices for vibration isolation applications: a review, Adv. Struct. Eng. 23 (8) (2020) 1739–1755.
[27] C. Liu, W. Zhang, K. Yu, T. Liu, Y. Zheng, Quasi-zero-stiffness vibration isolation: designs, improvements and applications, Eng. Struct. 301 (2024) 117282.
[28] J.-J. Lu, W.-H. Qi, F.-R. Liu, Y.-B. Cao, T.-Y. Zhao, L.-Q. Cai, Y. Li, G. Yan, W.-M. Zhang, Compliant curved beam support with flexible stiffness modulation for near-zero frequency vibration isolation, J. Sound Vib. 595 (2025) 118702.
[29] Y. Chai, J. Bian, M. Li, A novel quasi-zero-stiffness isolation platform via tunable positive and negative stiffness compensation mechanism, Nonlinear Dyn. 112 (1) (2024) 101–123.
[30] S. Zuo, D. Wang, Y. Zhang, Q. Luo, An innovative design of parabolic cam-roller quasi-zero-stiffness isolators for ultralow frequency vibration isolation, Nonlinear Dyn. 112 (21) (2024) 18717–18744.
[31] G.L. Holst, G.H. Teichert, B.D. Jensen, Modeling and experiments of buckling modes and deflection of fixed-guided beams in compliant mechanisms, J. Mech. Des. 133 (5) (2011).
[32] H. Fan, L. Yang, Y. Tian, Z. Wang, Design of metastructures with quasi-zero dynamic stiffness for vibration isolation, Compos. Struct. 243 (2020) 112244.
[33] Q. Zhang, D. Guo, G. Hu, Tailored mechanical metamaterials with programmable quasi-zero-stiffness features for full-band vibration isolation, Adv. Funct. Mater. 31 (33) (2021) 2101428.
[34] G. Radaelli, J. Herder, A monolithic compliant large-range gravity balancer, Mech. Mach. Theory 102 (2016) 55–67.
[35] F. Ma, G. Chen, H. Wang, Large-stroke constant-force mechanisms utilizing second buckling mode of flexible beams: evaluation metrics and design approach, J. Mech. Des. 142 (10) (2020) 103303.
[36] L. Xiao, X. Sun, L. Cheng, X. Yu, A 3D-printed quasi-zero-stiffness isolator for low-frequency vibration isolation: modelling and experiments, J. Sound Vib. 577 (2024) 118308.
[37] S. Hou, J. Wei, A quasi-zero stiffness mechanism with monolithic flexible beams for low-frequency vibration isolation, Mech. Syst. Signal Process. 210 (2024) 111154.
[38] S. Dalela, P. Balaji, D. Jena, Design of a metastructure for vibration isolation with quasi-zero-stiffness characteristics using bistable curved beam, Nonlinear Dyn. 108 (3) (2022) 1931–1971.
[39] C. Cai, J. Zhou, L. Wu, K. Wang, D. Xu, H. Ouyang, Design and numerical validation of quasi-zero-stiffness metamaterials for very low-frequency band gaps, Compos. Struct. 236 (2020) 111862.
[40] S. Guo, R. Gao, X. Tian, S. Liu, A quasi-zero-stiffness elastic metamaterial for energy absorption and shock attenuation, Eng. Struct. 280 (2023) 115687.

[41] J.-J. Lu, G. Yan, W.-H. Qi, H. Yan, J.-W. Shi, A. Chen, W.-M. Zhang, Load-adaptive quasi-zero stiffness vibration isolation via dual electromagnetic stiffness regulation, J. Sound Vib. 567 (2023) 118059.
[42] J. Winterflood, T. Barber, D. Blair, Using Euler buckling springs for vibration isolation, Class. Quantum Gravity 19 (7) (2002) 1639–1645.
[43] G. Leandri, A. Sunderland, J. Winterflood, L. Ju, Six degrees of freedom vibration isolation with Euler springs, Rev. Sci. Instrum. 92 (2) (2021).
[44] H. Gu, H. Ji, S. Zhang, C. Zhai, M. Xu, Displacement sensing with quasi-zero stiffness structure and flexoelectricity, Smart Mater. Struct. 32 (3) (2023) 035024.
[45] A. Cazzolli, F. Dal Corso, The elastica sling, Eur. J. Mech. A/Solids 105 (2024) 105273.
[46] L.L. Howell, Introduction to compliant mechanisms, in: L.L. Howell, S.P. Magleby, B.M. Olsen (Eds.), Handbook of Compliant Mechanisms, Wiley Online Library, 2013, pp. 1–13.
[47] A. Zhang, G. Chen, A comprehensive elliptic integral solution to the large deflection problems of thin beams in compliant mechanisms, J. Mech. Robot. 5 (2) (2013) 021006.
[48] J. Valle, D. Fernández, J. Madrenas, Closed-form equation for natural frequencies of beams under full range of axial loads modeled with a spring-mass system, Int. J. Mech. Sci. 153 (2019) 380–390.
[49] I.-D. Sîrbu, D. Preninger, D. Danninger, L. Penkner, R. Schwödiauer, G. Moretti, N. Arnold, M. Fontana, M. Kaltenbrunner, Electrostatic actuators with constant force at low power loss using matched dielectrics, Nat. Electron. 6 (11) (2023) 888–899.
[50] Mylar Specialty Films, Mylar® a technical datasheet, Mylar Specialty Films, May 2024, Technical datasheet, [Online]. Available: https://mylar.com/wp-content/uploads/2025/08/mylar_a-1.pdf (dated 8 May 2024).